

Citation for published version:

Yang, Y, Ohnoute, L, Ajmal, S, Zheng, X, Feng, Y, Li, K, Wang, T, Deng, Y, Liu, Y, Dong, X, Valev, V & Zhang, L 2019, "Hot Edges" in Inverse Opal Structure Enable Efficient CO₂ Electrochemical Reduction and Sensitive in-situ Raman Characterization', *Journal of Materials Chemistry A*, vol. 7, no. 19, pp. 11836-11846.
<https://doi.org/10.1039/C9TA02288K>

DOI:

[10.1039/C9TA02288K](https://doi.org/10.1039/C9TA02288K)

Publication date:

2019

Document Version

Peer reviewed version

[Link to publication](#)

All data supporting this research is openly available from the University of Bath Research Data Archive at <https://doi.org/10.15125/BATH-00792>.

University of Bath

Alternative formats

If you require this document in an alternative format, please contact:
openaccess@bath.ac.uk

General rights

Copyright and moral rights for the publications made accessible in the public portal are retained by the authors and/or other copyright owners and it is a condition of accessing publications that users recognise and abide by the legal requirements associated with these rights.

Take down policy

If you believe that this document breaches copyright please contact us providing details, and we will remove access to the work immediately and investigate your claim.

“Hot Edges” in Inverse Opal Structure Enable Efficient CO₂ Electrochemical Reduction and Sensitive *in-situ* Raman

Characterization

Yang Yang^{a,b}, Lukas Ohnouteck^{c,d}, Saira Ajmal^a, Xiuzhen Zheng^a, Yiqing Feng^a, Kejian Li^a, Tao Wang^a, Yue Deng^a, Yangyang Liu^a, Xu Dong^a, Ventsislav K. Valev^{c,d,*}, Liwu Zhang^{a,b,*}

^a*Department of Environmental Science and Engineering, Fudan University; Shanghai, 200433, P. R. China.*

^b*Shanghai Institute of Pollution Control and Ecological Security, Shanghai, 200092, Peoples' Republic of China*

^c*Centre for Photonics and Photonic Materials, University of Bath, Bath, BA2 7AY, United Kingdom*

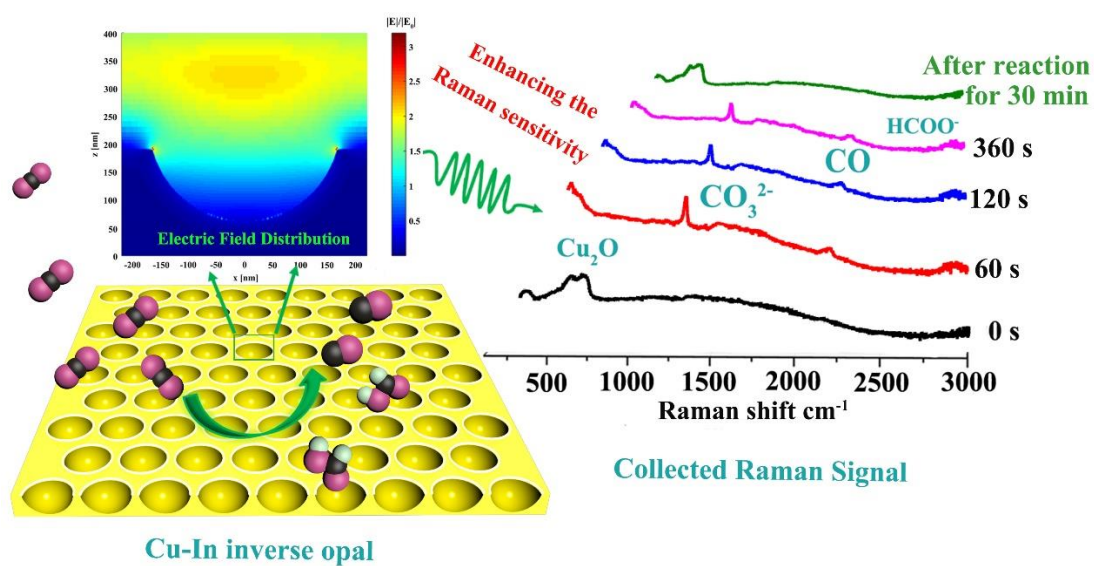
^d*Centre for Nanoscience and Nanotechnology, University of Bath, Bath, BA2 7AY, United Kingdom*

E-mail: zhanglw@fudan.edu.cn; v.k.valev@bath.ac.uk

Abstract:

Conversion of CO₂ into fuels and chemicals via electroreduction has attracted significant interest. Via mesostructure design to tune the electric field distribution in the electrode, it is demonstrated that Cu-In alloy with inverse opal (CI-1-IO) structure provides efficient electrochemical CO₂ reduction and allows for sensitive detection of the CO₂ reduction intermediates via surface-enhanced Raman scattering. The significant enhancement of Raman signal of the intermediates on CI-1-IO surface can be attributed to electric field enhancement on the “hot edges” of the inverse opal structure. Additionally, a highest CO₂ reduction Faradaic efficiency (FE) of 92% (sum of formate and CO) is achieved at -0.6 V vs. RHE on CI-1-IO electrode. The DRIFTS results show that the Cu-In alloy with inverse opal have a faster adsorption kinetic and higher adsorption capacity of CO₂. The “hot edges” of the bowl-like structure concentrate electric fields, due to the high curvature and also concentrate K⁺ on the active sites, which can lower the energy barrier of the CO₂ reduction reaction. This research provides new insight into the design of materials for efficient CO₂ conversion and the intermediates detection during CO₂ reduction processes.

TOC Graphic



“Hot Edges” in Cu-In monolayer inverse opal structure lead to ultrasensitive Raman signal of the intermediate and efficient electrochemical CO₂ reduction performance.

1. Introduction

Electrochemical reduction of carbon dioxide (CO₂) is a promising way to convert CO₂ to carbon-based fuels and chemicals using renewable electricity.¹⁻⁵ However, its application often suffers from the low conversion efficiency, poor selectivity and the lesser-known intermediates.^{3, 6} Consequently, substantial efforts have been dedicated to designing electrodes with efficient CO₂ reduction activity, such as controlling size and morphology, tuning electrolyte, introducing metal-oxide interfaces and fabricating porous structure etc.^{1, 7-13} By coupling another metal species to form alloy might reconstruct the catalyst interface, which could change the binding energy of intermediates on the surface during CO₂ reduction reaction resulting in controllable selectivity.¹⁴⁻²¹ Yet another method to facilitate CO₂ reduction efficiency and selectivity consists in introducing inverse opal structure.^{22, 23} Surendranath's group have designed Au and Ag inverse opal thin films with different thickness, which show a significant diminution of HER with increasing porous thin film thickness.^{22, 23} A Cu inverse opal structure derived from Cu₂O inverse opal was reported to show improved catalytic activity and selectivity of CO₂ electrochemical reduction due to the porous structure.²⁴ However, previous work on inverse opal mainly focused on the effects of diffusional gradients within the pores, while many of the specific property of inverse opal structures remain unexplored; such important properties include photonic Bragg resonances, electric field concentrations on the edge of the mesostructure and their potential effects for CO₂ reduction and *in-situ* measurements.

In-situ measurements have been playing an increasingly important role in the study of the CO₂ reduction mechanism. Such measurements include *in-situ* Raman spectroscopy, *in-situ* attenuated total reflectance-fourier transform infrared spectroscopy (ATR-FTIR), vibrational sum-frequency generation spectroscopy (VSFG), and operando extended X-ray absorption fine structure (EXAFS) etc.^{14, 16, 25-30} Among these measurements, *in-situ* Raman spectroscopy is an efficient and simple method for detecting the intermediates during CO₂ reduction.³¹⁻³⁹ However,

the Raman signal of the intermediates is very weak, which makes the signal hard to detect.^{16, 27} Generally, the typical electrochemical Raman cell contains electrodes, an electrolyte layer and a quartz window. The low sensitivity of Raman spectroscopy can be attributed to the limited optical path and mismatch of media.⁴⁰ Using an immersion objective with long working distance reduces the loss of Raman signal and improves the detection sensitivity, the spatial resolution, and the electrochemical response.^{23, 40, 41} However, this approach is usually expensive and complex. Nanostructure-based surface enhanced Raman spectroscopy (SERS) is also an effective method for surface analysis,⁴² which achieves ultrahigh sensitivity down to a single molecule level by utilizing coinage-metal (such as Au, Ag and Cu) nanostructures.^{42, 43} Developing electrodes with both good SERS ability and catalytic activity for *in-situ* investigation of the process of CO₂ reduction still presents a challenge.

Herein, by depositing a monolayer of inverse opal structured Cu-In alloy, we present a system, rich on “hot edges” for CO₂ reduction and *in-situ* Raman investigation. The Raman signal is dramatically enhanced compared to the case when a Cu-In alloy without inverse opal structure is used. Furthermore, the current density, FE_{HCOO⁻} and FE_{CO} are also significantly improved by introducing the inverse opal structure. The DRIFTS results demonstrate that CI-1-IO with inverse opal structure exhibit a faster adsorption kinetic and higher capacity for CO₂ adsorption, which might benefit for the CO₂ conversion. The greatly enhanced Raman signal is attributed to local field enhancements, demonstrated by finite-difference time-domain (FDTD) simulations. This Raman signal then enables the *in-situ* study of the CO₂ reduction process. The high-curvature structure concentrates electric fields, thus K⁺ gather on the active sites (“hot edges”). Density functional theory (DFT) calculations further demonstrate that the adsorbed K⁺ lower the energy barrier of the CO₂ reduction reaction (CO₂RR), which facilitates the CO₂ conversion.

2. Experimental

2.1 Chemicals

Styrene (Aldrich, 99%) and $K_2S_2O_8$ (AR, Sinopharm Chemical Reagent Co., China) were used to prepare polystyrene (PS) opal templates. Formic acid and Acetic acid standard sample (Sigma), $NaHCO_3$ and $NaCO_3$ (Sigma, 99%) were used for Ion Chromatograph (IC). The other reagents were purchased from Sinopharm Chemical Reagent Co., China. Fluoride-Tin Oxide (FTO) glasses (thickness, 1 mm) were purchased from China Southern Glass Co. Ltd. All chemical reagents are analytical grade and used without any further purification. Deionized (DI) water was used throughout the whole experiment. FTO glasses were sonicated while being immersed in piranha solution, ethanol and DI water in sequence to remove the impurities on the surface.

2.2 Preparation of polystyrene spheres

Monodisperse polystyrene spheres with diameter of about 360 nm were synthesized according to the process reported in the literature.⁴⁴ Typically, 100 mL of ultrapure water (18 $M\Omega/cm^2$) and 0.6 g styrene (washed by 5% NaOH solution to remove the polymerization inhibitor) were added into a three-necked, round-bottomed flask (250 mL). The mixture was stirred at 500 rpm, while being heated to 70 °C and purged with nitrogen gas with a flow rate of 70 mL/min. Afterwards, the mixture was kept at 70 °C for 20 min, 0.12 g of $K_2S_2O_8$ was added and kept for 12 h. The oversize and undersize particles of the precursor solutions of polystyrene (PS) microspheres were removed by high-speed centrifugation. A first centrifugation was used to remove the undersize PS microspheres and a second one to remove the oversize PS microspheres. At the end of the process, the average particle diameter of the PS microspheres was approximately 360 nm.

The concentration of PS spheres was diluted to 0.03% (mass fraction) using DI water. Subsequently, the FTO glass was immersed vertically into the PS colloid solution. Then, the solution with the glass was placed in a furnace and kept at 55 °C until the water entirely

evaporated. The PS opal templates self-assembled on the FTO with a close-packing structure, named as FTO-PS.

2.3 Preparation of CuIn film with and without inverse opal structure

Cu-In alloy was prepared by an electrodeposition method reported by Yuan et al. with a minor modification.⁴⁵ Firstly, 5 mmol $\text{CuCl}_2 \cdot 2\text{H}_2\text{O}$, was added into the solution containing 0.2 mmol triethanolamine and 0.015 mmol sodium citrate. Then, 5 mmol $\text{InCl}_3 \cdot 4\text{H}_2\text{O}$ was added into the solution. Finally, the pH of solution was adjusted to 4 using H_2SO_4 and NaOH .

2.3.1 Preparation of Cu-In film without inverse opal structure

FTO conductive glass, saturated calomel electrode and platinum foil were used as working electrode, reference electrode and counter electrode, respectively. Electrodeposition was conducted at -1 V (*vs.* SCE) for 30 min at 30 °C. The sample was named CI-1.

2.3.2 CuIn film with inverse opal structure (CI-1-IO)

For the CI-1-IO preparation, FTO-PS was used as the working electrode and the other electrodeposition conditions were kept the same as for CI-1. After electrodeposition, the sample was dried in air flow, then immersed into tetrahydrofuran (THF) solution for 30 min to remove the PS template. Later, the sample was washed by ethanol and water. We designate this sample: CI-1-IO. Scheme S1 (electronic supplementary information, ESI) illustrates the preparation procedure of polystyrene (PS) opal template and the CI-1-IO sample.

2.4 Characterization

The X-ray diffraction (XRD) patterns were measured using a Bruker D8 Advance X-ray diffractometer with Cu K radiation. The accelerating voltage and applied current were 40 kV and 40 mA, respectively. The general morphology imaging and element mapping of the samples were conducted using a field emission scanning electron microscopy (FESEM, Sigma Zeiss 150, Cal Zeiss Co., Germany) instrument operated at 5 kV and scanning transmission electron

microscopy (STEM, Phenom ProX, at 15 kV) with energy-dispersive spectroscopy (EDS). The photoelectrochemical data was collected using an IVIUM electrochemical workstation. The *in-situ* diffuse reflectance infrared fourier transform spectroscopy (DRIFTS) spectra were collected on a Shimadzu Tracer-100 FTIR spectrometer equipped with a high-sensitivity mercury cadmium telluride (MCT) detector cooled by liquid nitrogen. A temperature controller was coupled with the DRIFTS chamber (Praying Mantis Kit, Harrick). Samples were placed in a ceramic sample cup (0.35 mm depth, 5 mm i.d.). A series of spectra were recorded every 2 minutes with 100 scans averaged for each spectrum and a resolution of 4 cm^{-1} . The *in-situ* Raman spectra were measured on an XploRA confocal spectrometer (Jobin Yvon, Horiba Gr, France) with a charge coupled device (CCD) detector. Raman scattering was excited by an external-cavity diode laser (785 nm, with 25% energy) coupled with a 10 \times Olympus microscope objective. A holographic notch filter was equipped to filter out the excitation line and a holographic grating (1200 gr/mm) was employed for spectral mapping. A CCD with 1024 \times 256 pixels was used to collect the spectra in a resolution of 1.2 cm^{-1} , with 2 accumulations at 2 s acquisition time.

2.5 Electrochemical reduction of CO_2

All electrochemical measurements were carried out on an IVIUM electrochemical workstation in a conventional three-electrode system. A platinum plate and an Ag/AgCl electrode were used as the counter and reference electrodes, respectively. The anode and cathode compartment of electrochemical cell were separated by a Nafion 117 membrane. Before the measurement, CO_2 was bubbled into 50 ml electrolyte of x ($x = 0.1, 0.2, 0.5$ and 1.0) M KHCO_3 solution for 30 minutes to reach the saturation. The gas products were analyzed by gas chromatography (SHIMADZU, GC-2014) equipped with TDX-1 and HT-POLT $\text{Al}_2\text{O}_3/\text{S}$ columns. A thermal conductivity detector (TCD) was mainly used to detect and quantify H_2 , a flame ionization detector (FID) with methanizer was used to analyze and quantify CO by TDX-

1 column, and another FID was used for separating and quantifying CH₄ and other alkane contents with a HT-POLT Al₂O₃/S column. Ar (99.999%) was used as carrier gas. Liquid products were analyzed by Ionic chromatography (IC, Metrohm, 883 Basic IC Plus with Metrosp A SUPP 5-250 column) and ¹H nuclear magnetic resonance (NMR, AVANCE III HD, 500MHz, Bruker) spectrum. In order to confirm the organic products in solution, 0.5 ml liquid production was mixed with 0.1 mL D₂O containing 0.01 uL DMSO as the internal standard for a one-dimensional ¹H NMR spectrum test. Typically, the peak at about 8.3 ppm corresponding to the formic acid (HCOOH) and the peak at ~ 2.6 ppm present the dimethyl sulfoxide (DMSO). To quantify the HCOOH, the solution was diluted 10 times with ultrapure water, then injected into IC. Data are shown in the ESI (Fig. S14-S16).

2.6 Density functional theory (DFT) calculations on Cu₂In surface

DFT calculations were performed with Vienna *ab initio* Simulation Package (VASP) using the projector augmented wave (PAW) method with the exchange-correlation functional of Perdew-Burke-Ernzehr (PBE) and generalized gradient approximation (GGA).^{3, 46-48} The (001), (010), (100) and (110) slabs of Cu₂In were constructed by 4 × 4 × 1 supercell and separated by 12 Å of vacuum. The PAW pseudopotentials were used to calculate the interaction between ions and electrons in a plane wave basis set with a cut-off energy of 500 eV and a 4 × 4 × 1 k-points. The Gibbs free energies (ΔG) were calculated at 298.15 K and 1 atm, as outlined below:⁴⁹

$$G = H - T\Delta S = E_{DFT} + E_{ZPE} + \int_0^{298.15} C_v dT - T\Delta S$$

Where E_{DFT} is the optimized total energy, E_{ZPE} is the zero-point vibrational energy, $\int_0^{298.15} C_v dT$ is the heat capacity, H is enthalpy, T is the temperature and ΔS entropy. The change in ΔG between reaction steps of CO₂ to CO reaction coordinate was calculated from the computational hydrogen electrode model.⁵⁰ Moreover, the binding energy was calculated from DFT-optimized structures as follows: $E_{Binding} = E_{CO_2^*} - (E_{Cu_2In} + E_{CO_2})$, where

$E_{CO_2^*}$ is the energy of system with CO_2 proximate to the Cu_2In surface, E_{Cu_2In} is the energy of the Cu_2In surface (with and without K^+ for the respective cases) and E_{CO_2} is the energy of CO_2 gas.

2.7 FDTD and COMSOL simulations

For these simulations, the Lumerical FDTD (Finite Difference Time Domain) software was used to calculate the electric fields in the vicinity of the nanostructured surface of the sample CI-1-IO. Simulations were performed for a hexagonal arrangement of the bowl-like structures on the surface. Periodic boundary conditions were applied on the edges of the unit cell. It was assumed that the patterned layer consisted of Cu_2In alloy. The permittivity spectra of the alloy were calculated using Bruggeman effective medium approximation. In the model, the structures were irradiated with a linearly polarized broadband optical pulse and the electric field on the surface and in the longitudinal section was monitored.

Simulations of the free electron density on the working electrode with inverse opal structure were performed with the COMSOL Electric Currents module. The simulated system consisted of two electrodes separated with electrolyte. Voltage was applied between the two electrodes. In these simulations, the separation of the electrodes was chosen to be $1\ \mu m$ and the electrodes were simulated as made of Cu. The electric conductivity of the electrolyte was approximated as $2\ S\ m^{-1}$. The COMSOL calculations thus provide a good qualitative insight into the behavior of the working electrode during the CO_2 reduction process.

3. Results and discussion

3.1. Characterization of catalysts

The detailed steps for synthesizing Cu-In inverse opal (CI-1-IO) is shown in Scheme S1 (described in ESI). The X-ray diffraction (XRD) patterns of FTO, CI-1, and CI-1-IO are shown in Fig. 1a, suggesting the hexagonal-phase Cu_2In alloy (JPCDS No. 42-1475, with lattice parameters of $a=b=0.4294$ nm, $c=0.5233$ nm) is obtained. Any peaks from impurities of Cu_xO can hardly be seen in the XRD pattern of CI-1-IO. The morphology of the CI-1-IO sample is shown in Fig. 1b, which shows monolayer inverse opal structure (see also Fig. S1). Fig. 1c and d displays the image of an area selected for the energy-dispersive spectroscopy analysis and the total element mapping, respectively. From Fig. 1e to h, it is obvious that the Cu and In elements are distributed on the rim and O, Sn elements from the FTO glass are distributed in the center, which indicates that a monolayer inverse opal structure is formed. The EDX spectra confirm the presence of Cu and In in CI-1 (Fig. S2a) and Cu, In, Sn and O in CI-1-IO (Fig. S2b). The morphology and element mapping of planar CI-1 were also studied and presented in Fig. S1. X-ray photoelectron spectroscopy (XPS) analysis suggested all the three peaks of In^0 , Cu^0 and Cu_2O are detected on both CI-1 and CI-1-IO electrodes as shown in Fig. S3. Interestingly, Sn 3d5 spectra can be detected by XPS on the sample CI-1-IO, while it can hardly be observed on the CI-1 suggesting an inverse opal structure is formed on CI-1-IO. From Fig. 1a and S1, it can be seen that for CI-1, the surface of the FTO glass is completely covered by the Cu-In nanoparticles. Therefore, no Sn 3d5 peak is observed for the CI-1 sample. The specific analyses of elements are described below Fig. S3.

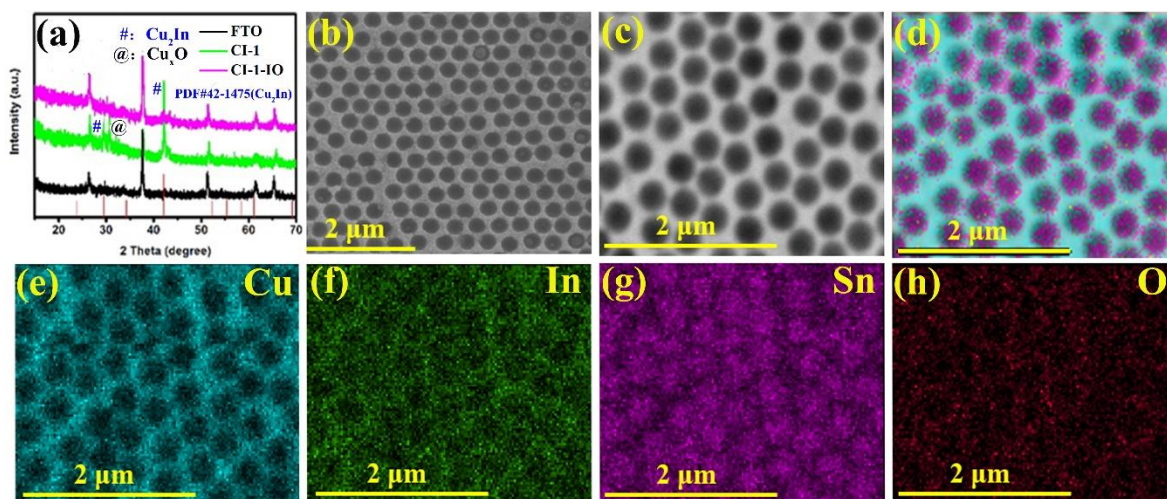


Fig. 1. a) XRD patterns of FTO glass, CI-1 and CI-1-IO. b) STEM of CI-1-IO. c) Selected area for EDS and d) Element mappings of CI-1-IO in the rectangular region shown in c. e-h) Separated element mappings of Cu, In, Sn and O in the region shown in d, respectively.

The roughness factors (RF) of the samples were determined from a capacitance measurement (details are shown in ESI).^{51, 52} The steady state Cyclic voltammetry (CV) curves and corresponding capacitive scans of FTO, CI-1 and CI-1-IO are displayed in Fig. S4. The RF of the surface of the substrate (FTO) is taken as 1. The calculated RF of CI-1 and CI-1-IO is about 4.5 and 4.8, respectively. Besides, electrochemical impedance spectroscopy (EIS) was further used to investigate the charge transfer process at the electrode/electrolyte interface. The radius of CI-1-IO sample is smaller than that of CI-1 (Fig. S5), which means that the charge transfer resistance of CI-1-IO is smaller than that of CI-1.⁵³ In turn, it benefits the electron transfer. Tafel plots of CI-1 and CI-1-IO were studied as well (Fig. S6). The slopes of both CI-1 and CI-1-IO are greater than 120 mV dec⁻¹, indicating single-electron transfer is the rate-determining step on both two electrodes.⁵⁴

3.2 CO₂ reduction performances of CI-1 and CI-1-IO in H-cell.

CO₂ reductions on CI-1 and CI-1-IO electrodes were performed at different voltages in 0.1 M KHCO₃ solutions; the results are shown in Fig. 2. It is observed that the FE_{Formate} and FE_{CO} of CI-1-IO are significantly higher than that of the CI-1 catalyst (Fig. 2a and b), indicating that

inverse opal structure might suppress the H₂ evolution reaction (Fig. 2c) and simultaneously facilitate CO₂ conversion. The highest FE of formate (~ 75%) is achieved at -0.6 V *vs.* RHE on CI-1-IO, which is almost 2.7 times higher than that of CI-1 (~ 28%). Considering that the current density of CI-1-IO is also about 2 times higher than that of CI-1 (Fig. 2d), the production rate of formate on CI-1-IO is almost 5.4 times faster than that on CI-1. CI-1-IO catalyst exhibits much higher electrochemical CO₂ reduction FE than CI-1 catalyst, especially at low potentials. At -0.6 V *vs.* RHE, the highest FE for CO₂ reduction over CI-1-IO reaches ~ 92%, which is about 2.6 times higher than that of CI-1 (~ 36%). Therefore, the inverse opal structure not only increases the CO₂ conversion efficiency but also improves the product selectivity. The improved current density and product selectivity cannot be explained by the exposed FTO surface on the CI-1-IO sample, as our experiments using pure FTO showed very low activity for the CO₂ electrochemical reduction (Fig. S7). As the CI-1 and CI-1-IO possess a similar electrode RF of 4.5 and 4.8, the difference in the surface area of the electrodes cannot be the only reason for the improved activity.

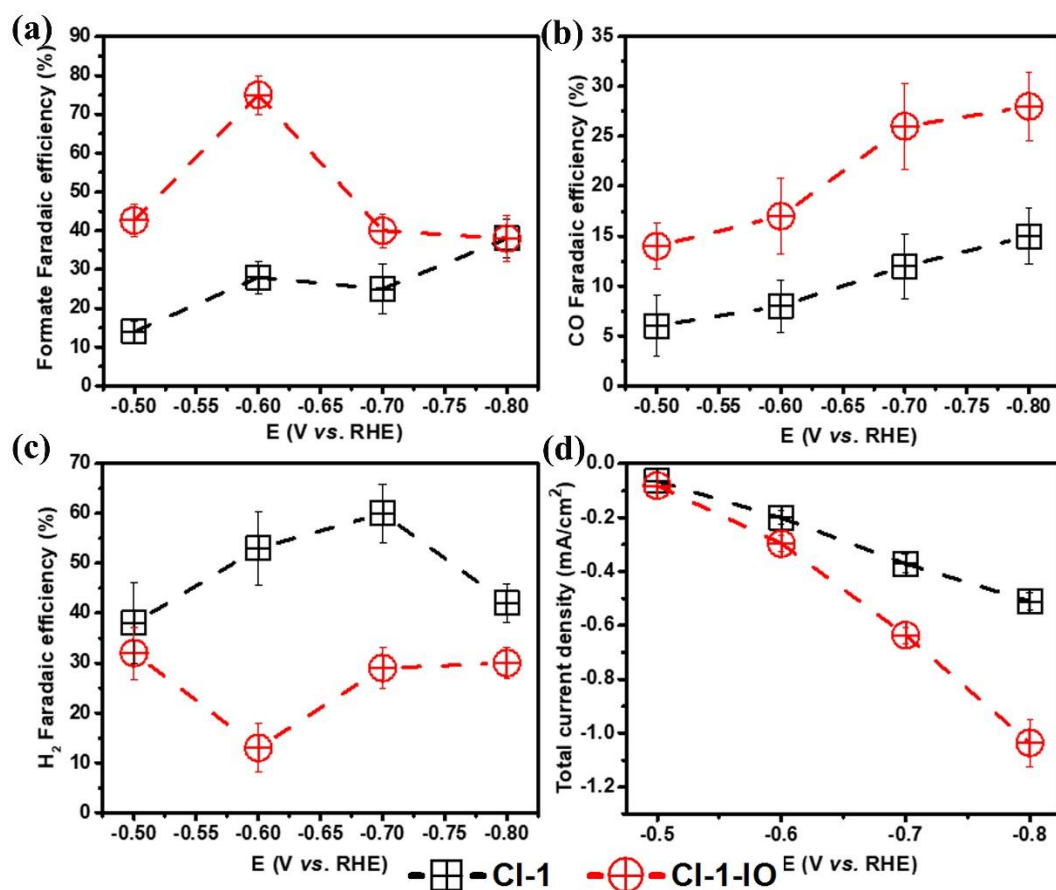


Fig. 2. Faradaic efficiency (FE) of a) HCOO^- , b) CO and c) H_2 . d) Total current density over CI-1 and CI-1-IO catalyst at CO_2 -saturated 0.1 M KHCO_3 solution. The error bar represents the standard deviation of three experiments.

3.3 Mechanism of enhanced CO_2 reduction selectivity and activity

We then further explored the mechanism of enhanced CO_2 reduction selectivity and activity via *in situ* technique and theoretical calculations. Surendranath and coworkers have designed Au and Ag inverse opal thin films with different thickness, the improved CO_2 reduction activity was attributed to the effects of diffusional gradients within the pores of inverse opal²²⁻²³. However, in this work the inverse opal has a monolayer structure (nanobowl array, no three-dimensional continuous pores), the effect of diffusion or mass transportation is thus weak. On one hand, the *in-situ* DRIFTS results demonstrate that the Cu-In alloy with inverse opal structure exhibits faster adsorption kinetics and higher capacity for CO_2 adsorption,

as shown in Fig. 3. CO₂ adsorption on the sample surface was studied by inducing a CO₂/H₂O mixture to the reaction cell with 10 mL/min flow rate in the dark. The data is collected every two minutes until the CO₂ adsorption peak is stable (about 28 min). The collected in situ DRIFTS spectrum are shown in Fig. 3 (see Fig. S8 for more details). The highest peak at about 2364 cm⁻¹ can be attributed to the CO₂ (gas-phase) adsorption on the sample surface, which show a fast adsorption equilibrium process (about 2 min) for the gas phase. From Fig. S8a, we can see that, after 28 min adsorption, the spectra region of 1000-1800 cm⁻¹ and 2688-3500 cm⁻¹ on CI-1-IO surface are obviously higher than that of CI-1 surface, indicating that the CI-1-IO with inverse opal structure have a higher adsorption ability than that of CI-1. The broad band at 2688-3500 cm⁻¹ correspond to the increased hydrogen bonding between the CO₂ adsorption products and hydroxyl groups on the Cu-In alloy surface.⁵⁵ The spectra region from 1000 to 1800 cm⁻¹ can be assigned to the adsorbed carbonate and bicarbonate, which are shown in detail in Fig. 3c and 3d (also shown in Fig. S8b and c), respectively. Specifically, the band at about 1227 and 1686 may be attributed to the δ_4 (COH) and ν_2 (OCO)_a of vibrational modes of the adsorbed bicarbonate.^{55, 56} It has been reported that the carbonate band usually appear at 1200-1700 cm⁻¹ and often observed as broad overlapping bands.⁵⁵ The band at about 1566 cm⁻¹ may correspond to the bidentate form of adsorbed carbonate, and the peak at 1057 and 1383 cm⁻¹ is associated with the monodentate form of carbonate, usually considered as ν_1 stretch.⁵⁵⁻⁵⁷ Notably, the intensity of the peaks of carbonate and bicarbonate increase with the increasing of CO₂ flow time shown in Fig. 3c and d, and after 28 min the intensity of the peaks of CI-1-IO is much stronger than that of CI-1. Specifically, the intensity changes of 1383 and 1227 cm⁻¹ are summarized in Fig. S3b. Additionally, the CO₂ adsorption performance on pre-wetted electrode surface in closed cell is also studied as well (shown in Fig. S9). Fig. S9 shows that the adsorbed gas-phase CO₂ (about 2366 cm⁻¹) was saturated for both CI-1 and CI-1-IO after 3 mins. Meanwhile, the CI-1-IO sample shows a higher adsorption capacity of gas-phase CO₂ than CI-1. More details are discussed in ESI. The strong adsorption intensity and fast adsorption

equilibrium process demonstrate CI-1-IO have a faster adsorption kinetic and higher capacity for CO₂ adsorption, which would benefit for the CO₂ conversion.

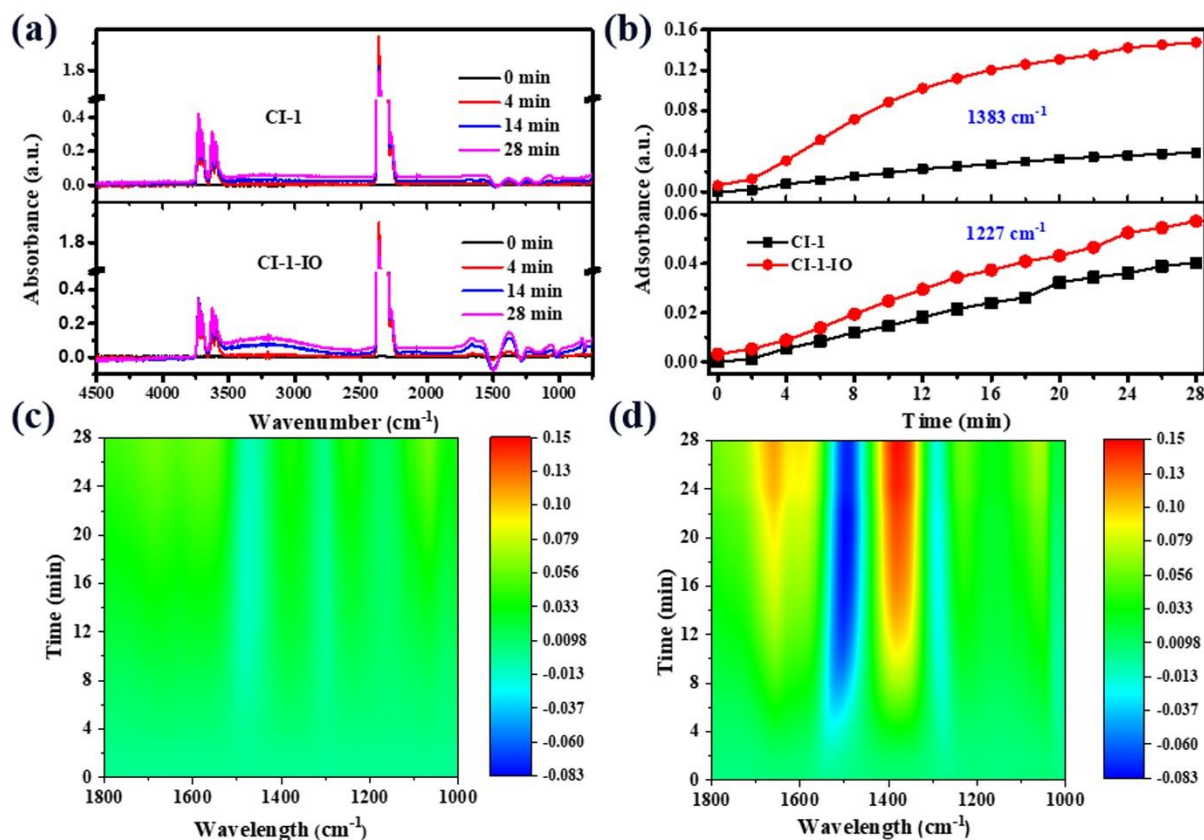


Fig. 3. *In-situ* DRIFTS spectra of CO₂/H₂O adsorbed on CI-1 and CI-1-IO surface. a) Whole spectra from 750-4500 cm⁻¹, 0 to 28 min. b) Intensity of specific peaks (1383 and 1227 cm⁻¹) of CI-1 and CI-1-IO. Spectra regions (1000-1800 cm⁻¹) of adsorbed carbonate on c) CI-1 and d) CI-1-IO surface.

On the other hand, the high-curvature structures in inverse opal can concentrate electric field, which affects the ion concentrations near the surface. To understand the mechanism of improved CO₂ reduction on CI-1-IO, we detected the local relative K⁺ concentration adsorbed on the electrodes by ion chromatography (IC) spectrometry. The concentration of K⁺ adsorbed on the electrode surface was measured by the reported method and shown in Fig. S10.³ It was found that the K⁺ concentration when CI-1-IO was used (50.3 mg L⁻¹) was about 2 times higher than in the case of CI-1 (24.5 mg L⁻¹).

The influence of K^+ on the CO_2RR was further studied via *Ab initio* molecular dynamics simulations. The Gibbs free energy of diagrams obtained from density functional theory (DFT) calculations on Cu_2In surface models of different facets at 298.15K, 1 atom and 0 V *vs.* RHE are shown in Fig. 4. The results indicate that the adsorbed K^+ ions can lower the thermodynamic energy barrier for reaction for all facets. On Cu_2In (001) facet (Fig. 4a), the adsorbed K^+ stabilizes the $COOH^*$ and $HCOOH^*$ intermediates by 1.21 and 1.82 eV, respectively. For Cu_2In (100) and (110) facet, the energy barrier of rate-determining $COOH^*$ is lowered by 0.75 and 0.73 eV with the presence of K^+ , respectively (Fig. 4b and c). Meanwhile, Fig. 4b and c show that adsorbed K^+ stabilizes the $HCOOH^*$ by 0.48 and 0.6 eV for the Cu_2In (100) and (110) surface, respectively. On the Cu_2In (010) surface (Fig. 4d), the adsorbed K^+ lowers the energy of $COOH^*$ and $HCOOH^*$ from 1.09 to 0.48 eV and 0.8 to 0.25, respectively. Simultaneously, the adsorbed K^+ ions also show an ability to lower the thermodynamic energy barrier for the production of CO for all facets (seeing Fig. S11) and the optimized structures for different Cu_2In facets with and without K^+ are shown in Fig. S12. Overall, the results show that the adsorbed K^+ might lower the reaction barrier of $COOH^*$, $HCOOH^*$ and CO^* intermediates which demonstrates that the adsorbed cations are beneficial for the CO_2 reduction.

Based on the results discussed above, it can be suggested that K^+ ions locally concentrated at the active sites enhance the CO_2RR . The high-curvature structures in an inverse opal can concentrate electric field, which affects the ion concentrations near the surface. Here, a finite-element numerical calculation is employed to study the enhanced field intensification caused by the inverse opal structure. The computed electric field near the sharp edges of the bowl structure is shown in Fig. 4e. The free electron density distribution on the edges of bowl structure is shown as a color map. The electrostatic field distribution around the edge of the bowl-like structure on the electrode is shown as a group of arrows, where the size and direction of each arrow represent the magnitude and the direction of the electric field. It can be seen that the edges of the bowl structure concentrate electrons. Additionally, a locally enhanced

electrostatic field is generated by the locally concentrated free electron density on the surface of the electrode and points towards the locally concentrated free electron density (arrows in the inset in Fig. 4e). The results can be explained by migration of free electrons to the regions of the highest curvature on a charged metallic electrode which is a consequence of electrostatic repulsion.

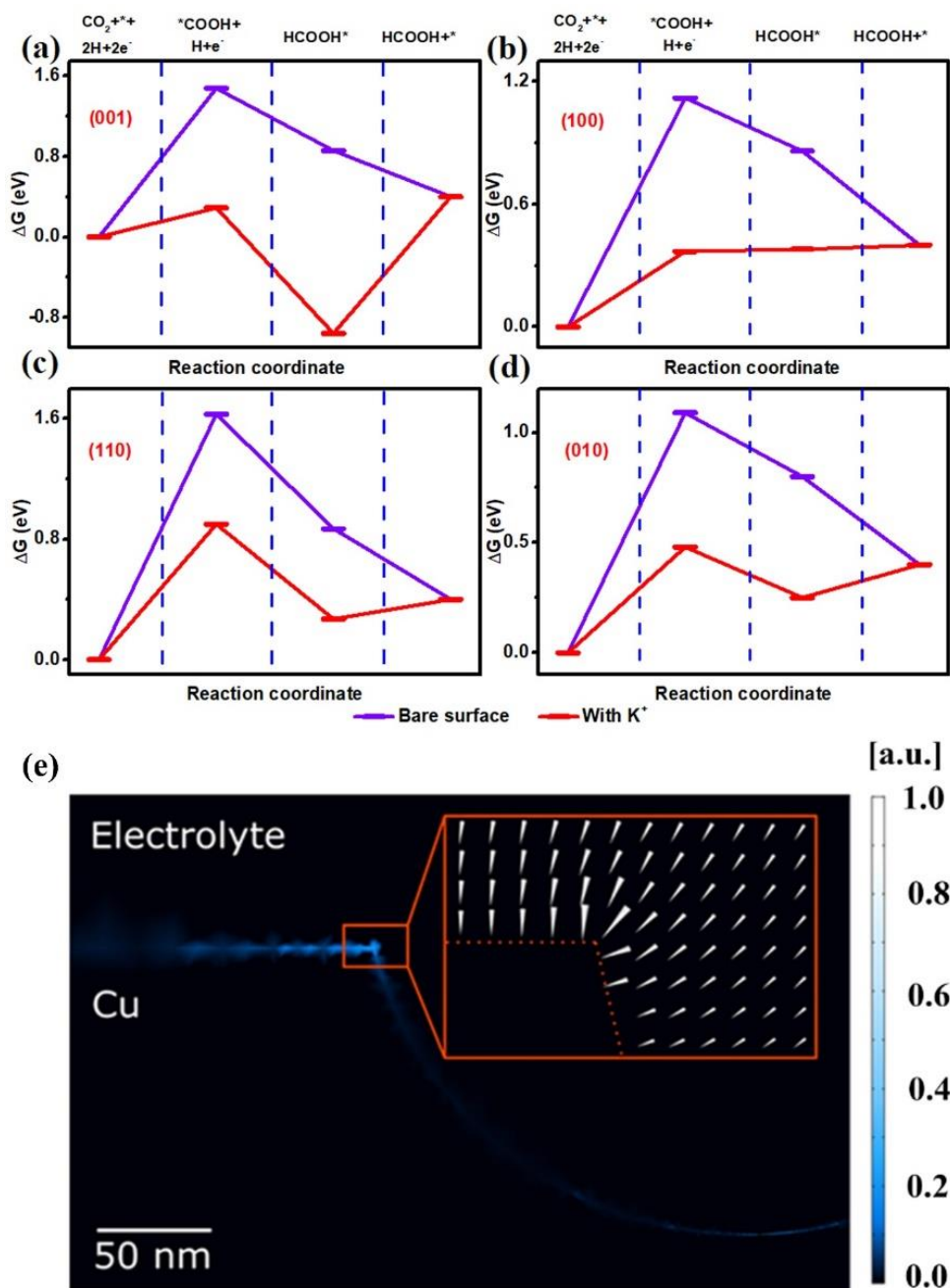


Fig. 4. Thermodynamic barriers for CO_2 to HCOOH reduction reaction on Cu_2In surface with and without K^+ . Gibbs free energy of electroreduction of CO_2 to HCOOH on Cu_2In a) (001), b)

(100), c (110) and d) (010) facets in the presence of adsorbed K^+ and without K^+ . e) Computed electron density and the electric field near the surface of the CI-1-IO electrode. The color map represents the normalized free electron density distributed on the surface of the material. The direction and the magnitude of the electrostatic field around the electrode is represented by the white arrows in the inset.

3.4 *In-situ* Raman investigation

Raman signal can also benefit from the inverse opal structure, which enhances local electric fields. It is thus of interest to use this structure for *in-situ* investigation of the reduction process of CO_2 via surfaced enhanced Raman spectroscopy. Fig. 5a-c show the *in-situ* Raman spectra obtained in a tailored cell (shown in Fig. S13) utilizing an electrolyte containing 7 ml CO_2 saturated 0.1 M $KHCO_3$ over the CI-1 and CI-1-IO electrodes at -0.7 V vs. RHE. The chemical composition of the prepared electrodes and their transformations during CO_2 electroreduction were elucidated by Raman spectroscopy (Fig. 5). In the microscopic image of CI-1-IO (Fig. 5a), we can see some bright spots on the electrode surface caused by the inverse opal structure. These are consistent with surface-enhancement of the Raman scattering signal from the chemical compounds on the surface. In Fig. 5b, it can be seen that the Raman signal of the reaction intermediates can hardly be identified on the CI-1 electrode without inverse opal structure, while the signal is much clearer when the CI-1-IO electrode is used, as shown in Fig. 5c. The Cu-In alloy with inverse opal structure has a SERS effect, which makes it easier to measure the Raman spectra. Before applying external voltage (at time = 0 s), the peaks at 219, 526 and 617 cm^{-1} can be assigned to Cu_2O .²³ Within 60 s of applying potential difference, the peaks (at 526 and 617 cm^{-1}) attributed to Cu_2O disappear, which indicates that the catalyst is in the metallic state. Meanwhile, the CO-related peak at 2075 cm^{-1} (CO stretching) appears. A strong signal at 1065 cm^{-1} is also observed, which can be assigned to the stretching mode of the adsorbed carbonate in the interfacial region.^{31, 35, 58} This signal was not observed in recent

reports.^{16, 23, 26, 33, 59} Up to now, it is poorly understood that how the carbonate form and whether it affect CO₂ reduction. One view is that carbonate adsorbed on the metal surface is thorough ionic bonds. Such a bond is formed by ligand exchange of HCO₃⁻ with adsorbed water/hydroxyl followed by deprotonation, which does not participate in the CO₂ reduction reaction.^{6, 35} Another viewpoint thought the carbonate is formed by activation of CO₂ on the surface oxygen/hydroxyl sites.⁶ There is another proposition (proved by the ATR-FTIR spectra) that CO₂ couple with CO₂⁻ intermediate firstly, then reduced by another electron resulting in CO and CO₃²⁻ formation.²⁷ The broad band at about 2900 cm⁻¹ can be assigned to the C-H stretching of the formate species.^{58, 60}

During the study time from 60 to 600 s, the signals of carbonate (1065 cm⁻¹) and CO (2075 cm⁻¹) stretching are steady, indicating that a balance of the reduction reaction is reached. When the voltage is removed for 3 min (the first red curve in Fig. 5c), the intensity of the carbonate and CO stretching signal decreases. The Cu₂O peaks appear again, while the carbonate and CO stretching signal decrease significantly after removing the voltage for 10 min. After removing the voltage for 30 min, the Raman spectrum returns to the original shape before reaction. Neither the signal from carbonate nor from CO stretching is observed. However, when the voltage is applied again for 30 s, the signal of Cu₂O disappears again, while the carbonate and the CO stretching mode peaks can be observed. After removing the potential for 30 min, the Raman spectrum is similar to the first round, indicating the repeatability of the Raman study. These operando Raman spectra demonstrate that the Cu₂O is rapidly reduced to the metallic state upon the application of voltage and then the CO₂ reduction reaction occurs on the metal surface. Interestingly, the reduced Cu reoxidizes to Cu₂O after removing the applied voltage. Both the CO₃²⁻ and CO intermediates (CO stretching) can be observed during the CO₂ reduction in the Raman spectra. The inverse opal structure enables more sensitive *in-situ* Raman study of the reaction process during CO₂RR.

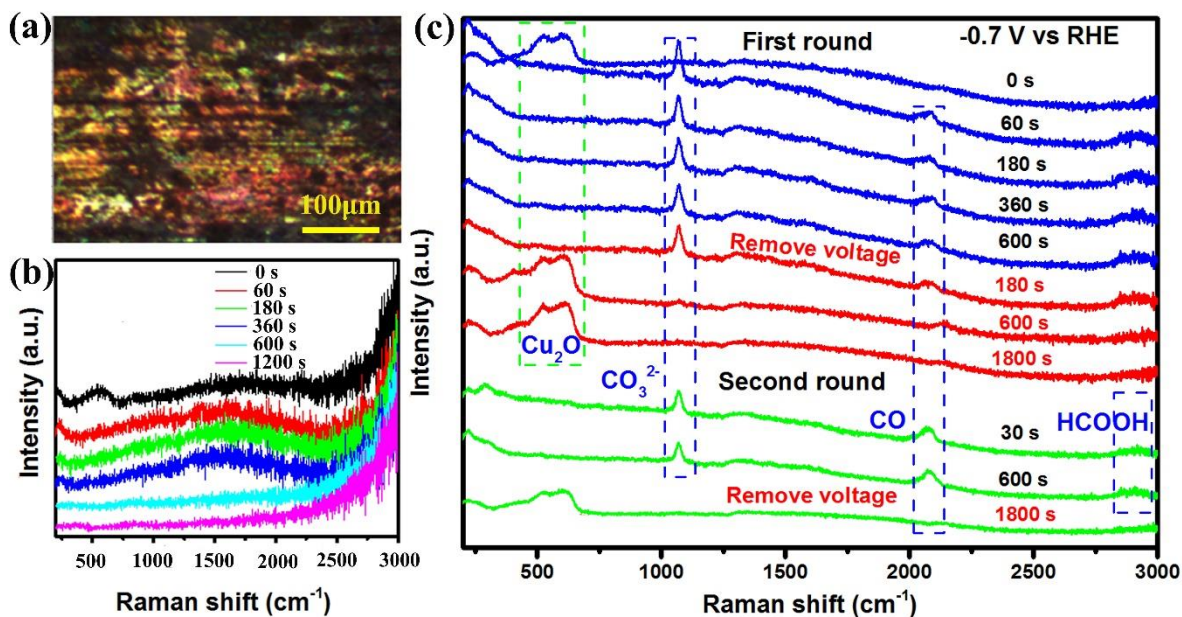


Fig. 5. a) Microscopic image of CI-1-IO. *In-situ* Raman spectra of b) CI-1 and c) CI-1-IO during CO₂ reduction at -0.7 V vs. RHE in 0.1 M KHCO₃.

To further understand the influence of the inverse opal structure on the electric field at the surface of the electrode, finite-difference time-domain (FDTD) method was used to calculate the electric field distribution on the Cu-In inverse opal structure when irradiated with light. Fig. 6a and b show the distribution of electric field (E-field) on the surface and the longitudinal profile of the field when the Cu-In monolayer with inverse opal structure is irradiated with 785 nm light. It can clearly be seen that the center of the cavity, the top and the sharp edges of the bowl structure show an enhanced E-field. Specifically, on the sharp edges of the bowl, the magnitude of the E-field is 2-4 times higher. It has been reported that a small increase in the local field can produce large enhancements in Raman scattering (the enhancement scales roughly as E^4).⁶¹ The enhanced Raman signal can also benefit from the improved production rate of CO and formate on CI-1-IO, which is 4.8 and 3.4 times faster than on CI-1 at -0.7 V vs. RHE. However, the Raman signal is improved significantly more than this, as seen in Fig. 5b. The Raman signal of the intermediates can hardly be observed on CI-1. Hence, the enhancement of Raman scattering can be mainly attributed to the enhanced electric field on the surface of the

inverse opal structure. The “hot edges” presents as an active site is also supported by previous report by Morimoto et al., who use open-loop electric potential microscopy (OL-EPM) prove that the edge site of porous Zn is the reactive site for CO₂ reduction.⁶² Additionally, their OL-EPM results show that the higher current concentration at the edge site is attribute to the increased electric field strength.

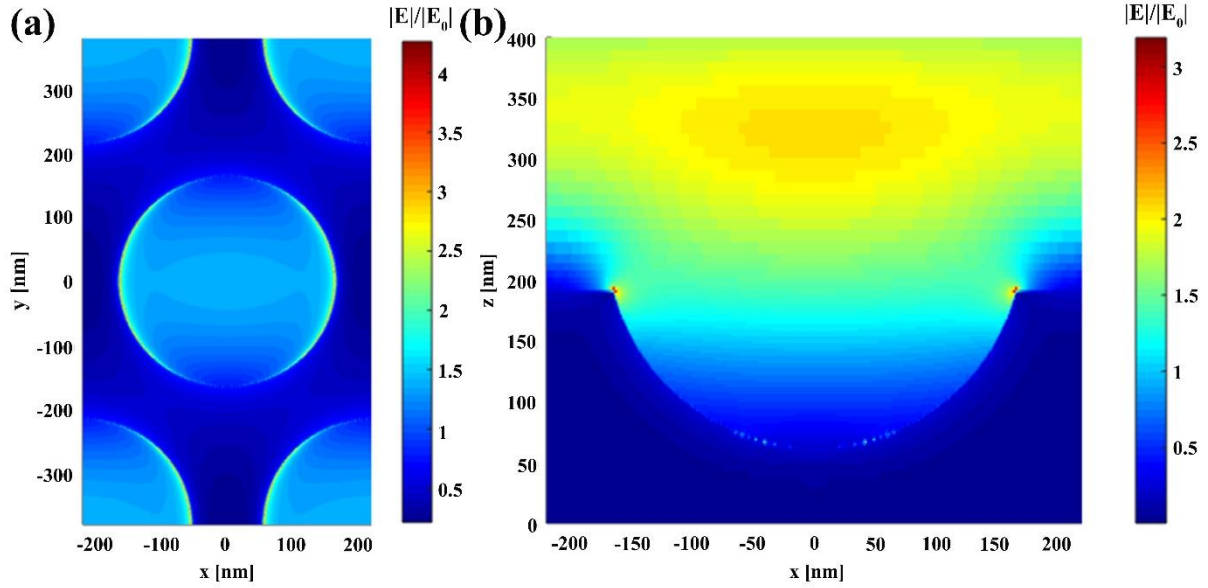


Fig. 6. Electric field distribution simulated for Cu-In inverse opal structure, when irradiated with 785 nm light, by a finite-difference time-domain (FDTD) method. The direction of light polarization is along x. In a), mapping of the electric field distribution on the surface. In b), mapping of the longitudinal profile of the electric field distribution.

4. Conclusions

In summary, we have successfully prepared a Cu-In alloy electrode with inverse opal structure possessing plenty of “hot edges” for CO₂ reduction and showed that it can be used *in-situ* to improve the sensitivity of Raman spectroscopy. The structure not only exhibits higher efficiency of CO₂ reduction, but also dramatically enhances the Raman spectra compared to Cu-In alloy without inverse opal structure. DRIFTS results display that the inverse opal structure has a faster adsorption kinetic and higher capacity for CO₂ adsorption, which would benefit for the CO₂ conversion. The Cu-In alloy electrode with inverse opal structure also concentrates electric fields due to the high curvature structure (COMSOL simulation), and thus concentrates K⁺ on the active sites, which lowers the thermodynamic energy barrier of the CO₂ reaction (DFT calculation) and reduces the mean square displacement of CO₂ relative to the surface. The characteristic peaks of the CO intermediate, carbonate and formate were observed on the CI-1-IO electrode. However, these peaks can hardly be observed on the CI-1 electrode. The enhanced Raman signal can be attributed to the inverse opal structure, which enhances the electric field on the sharp edges of the electrode (FDTD simulation). This work introduces “hot edges” structure as promising strategy for improving efficiency and selectivity of CO₂RR, this structure also enables sensitive *in-situ* detection of intermediates via SERS and thus provides a way to elucidate the exact mechanism of the electrochemical CO₂RR.

Conflicts of interest

There are no conflicts to declare.

Acknowledgements

The authors gratefully acknowledge financial support from the Ministry of Science and Technology of the People's Republic of China (2016YFE0112200), National Natural Science Foundation of China (No. 21507011 and No. 21677037). LO and VKV acknowledge funding and support from the Engineering and Physical Sciences Research Council (EPSRC) Centre for Doctoral Training in Condensed Matter Physics (CDT-CMP), Grant No. EP/L015544/1. VKV acknowledges support from the Royal Society through the University Research Fellowships and grants CHG\R1\170067, PEF1\170015 and RGF\EA\180228.

References

1. D. Gao, Y. Zhang, Z. Zhou, F. Cai, X. Zhao, W. Huang, Y. Li, J. Zhu, P. Liu and F. Yang, *J. Am. Chem. Soc.*, 2017, **139**, 5652-5655.
2. S. Gao, Y. Lin, X. Jiao, Y. Sun, Q. Luo, W. Zhang, D. Li, J. Yang and Y. Xie, *Nature*, 2016, **529**, 68-71.
3. M. Liu, Y. Pang, B. Zhang, P. De Luna, O. Voznyy, J. Xu, X. Zheng, C. T. Dinh, F. Fan, C. Cao, F. P. de Arquer, T. S. Safaei, A. Mepham, A. Klinkova, E. Kumacheva, T. Filleter, D. Sinton, S. O. Kelley and E. H. Sargent, *Nature*, 2016, **537**, 382-386.
4. Q. Lu, J. Rosen, Y. Zhou, G. S. Hutchings, Y. C. Kimmel, J. G. Chen and F. Jiao, *Nat. Commun.*, 2014, **5**, 3242.
5. J. Qiao, Y. Liu, F. Hong and J. Zhang, *Chem Soc Rev*, 2014, **43**, 631-675.
6. I. V. Chernyshova, P. Somasundaran and S. Ponnurangam, *Proc. Natl. Acad. Sci. U.S.A.*, 2018, **115**, E9261-E9270.
7. J. Rosen, G. S. Hutchings, Q. Lu, S. Rivera, Y. Zhou, D. G. Vlachos and F. Jiao, *ACS Catal.*, 2015, **5**, 4293-4299.
8. H. Kim, H. S. Jeon, M. S. Jee, E. B. Nursanto, J. P. Singh, K. Chae, Y. J. Hwang and B. K. Min, *ChemSusChem*, 2016, **9**, 2097-2102.
9. D. F. Gao, F. Cai, G. X. Wang and X. H. Bao, *Curr. Opin. Green. Sust.*, 2017, **3**, 39-44.
10. H. Zhou, Q. Chen, G. Li, S. Luo, T. B. Song, H. S. Duan, Z. Hong, J. You, Y. Liu and Y. Yang, *Science*, 2014, **345**, 542-546.
11. S. Back, M. S. Yeom and Y. Jung, *ACS Catal.*, 2015, **5**, 5089-5096.
12. G. O. Larrazábal, A. J. Martín, S. Mitchell, R. Hauert and J. Pérez-Ramírez, *ACS Catal.*, 2016, **6**, 6265-6274.
13. A. Jedidi, S. Rasul, D. Masih, L. Cavallo and K. Takanabe, *J. Mater. Chem. A*, 2015, **3**, 19085-19092.
14. Y. Zhou, F. Che, M. Liu, C. Zou, Z. Liang, P. De Luna, H. Yuan, J. Li, Z. Wang, H. Xie, H. Li, P. Chen, E. Bladt, R. Quintero-Bermudez, T.-K. Sham, S. Bals, J. Hofkens, D. Sinton, G. Chen and E. H. Sargent, *Nat. Chem.*, 2018, **10**, 974.
15. C. G. Morales-Guio, E. R. Cave, S. A. Nitopi, J. T. Feaster, L. Wang, K. P. Kuhl, A. Jackson, N. C. Johnson, D. N. Abram, T. Hatsukade, C. Hahn and T. F. Jaramillo, *Nat. Catal.*, 2018, **1**, 764-771.
16. T. T. H. Hoang, S. Verma, S. Ma, T. T. Fister, J. Timoshenko, A. I. Frenkel, P. J. A. Kenis and A. A. Gewirth, *J. Am. Chem. Soc.*, 2018, **140**, 5791-5797.
17. M. B. Ross, C. T. Dinh, Y. Li, D. Kim, P. De Luna, E. H. Sargent and P. Yang, *J. Am. Chem. Soc.*, 2017, **139**, 9359-9363.
18. D. Kim, C. S. Kley, Y. Li and P. Yang, *Proc. Natl. Acad. Sci. U.S.A.*, 2017, **114**, 10560-10565.
19. D. Kim, C. Xie, N. Becknell, Y. Yu, M. Karamad, K. Chan, E. J. Crumlin, J. K. Norskov and P. Yang, *J. Am. Chem. Soc.*, 2017, **139**, 8329-8336.
20. D. Kim, J. Resasco, Y. Yu, A. M. Asiri and P. Yang, *Nat Commun*, 2014, **5**, 4948.
21. Z. B. Hoffman, T. S. Gray, K. B. Moraveck, T. B. Gunnoe and G. Zangari, *ACS Catal.*, 2017, **7**, 5381-5390.
22. A. S. Hall, Y. Yoon, A. Wuttig and Y. Surendranath, *J. Am. Chem. Soc.*, 2015, **137**, 14834-14837.
23. Y. Yoon, A. S. Hall and Y. Surendranath, *Angew. Chem. Int. Ed. Engl.*, 2016, **55**, 15282-15286.
24. X. Z. Zheng, J. Han, Y. Fu, Y. Deng, Y. Y. Liu, Y. Yang, T. Wang and L. W. Zhang, *Nano Energy*, 2018, **48**, 93-100.
25. D. Ren, Y. L. Deng, A. D. Handoko, C. S. Chen, S. Malkhandi and B. S. Yeo, *ACS Catal.*, 2015, **5**, 2814-2821.

26. M. C. Figueiredo, I. Ledezma-Yanez and M. T. M. Koper, *ACS Catal.*, 2016, **6**, 2382-2392.
27. H. Sheng, M. H. Oh, W. T. Osowiecki, W. Kim, A. P. Alivisatos and H. Frei, *J. Am. Chem. Soc.*, 2018, **140**, 4363-4371.
28. H. Mistry, A. S. Varela, C. S. Bonifacio, I. Zegkinoglou, I. Sinev, Y. W. Choi, K. Kisslinger, E. A. Stach, J. C. Yang, P. Strasser and B. R. Cuenya, *Nat Commun*, 2016, **7**, 12123.
29. L. G. A. van de Water, S. K. Wilkinson, R. A. P. Smith and M. J. Watson, *J. Catal.*, 2018, **364**, 57-68.
30. S. Zhu, B. Jiang, W. B. Cai and M. Shao, *J. Am. Chem. Soc.*, 2017, **139**, 15664-15667.
31. G. Kumari, X. Zhang, D. Devasia, J. Heo and P. K. Jain, *ACS Nano*, 2018, **12**, 8330-8340.
32. D. Bohra, I. Ledezma-Yanez, G. Li, W. de Jong, E. Pidko and W. J. A. C. Smith, *Angew. Chem. Int. Ed. Engl.*, 2018, **130**, 1-6.
33. D. Ren, J. Fong and B. S. Yeo, *Nat. Commun.*, 2018, **9**, 925.
34. G. Neri, J. J. Walsh, G. Teobaldi, P. M. Donaldson and A. J. Cowan, *Nat. Catal.*, 2018, **1**, 952.
35. L. Mandal, K. R. Yang, M. R. Motapothula, D. Ren, P. Lobaccaro, A. Patra, M. Sherburne, V. S. Batista, B. S. Yeo, J. W. Ager, J. Martin and T. Venkatesan, *ACS Appl. Mater. Interfaces*, 2018, **10**, 8574-8584.
36. Y. Huang, C. W. Ong and B. S. Yeo, *ChemSusChem*, 2018, **11**, 3299-3306.
37. D. Ren, B. S.-H. Ang and B. S. Yeo, *ACS Catal.*, 2016, **6**, 8239-8247.
38. Y. Deng, A. D. Handoko, Y. Du, S. Xi and B. S. Yeo, *ACS Catal.*, 2016, **6**, 2473-2481.
39. Y. Kwon, Y. Lum, E. L. Clark, J. W. Ager and A. T. Bell, *ChemElectroChem*, 2016, **3**, 1012-1019.
40. Z. C. Zeng, S. Hu, S. C. Huang, Y. J. Zhang, W. X. Zhao, J. F. Li, C. Jiang and B. Ren, *Anal. Chem.*, 2016, **88**, 9381-9385.
41. Y. L. Deng and B. S. Yeo, *ACS Catal.*, 2017, **7**, 7873-7889.
42. S. Y. Ding, J. Yi, J. F. Li, B. Ren, D. Y. Wu, R. Panneerselvam and Z. Q. Tian, *Nature Reviews Materials*, 2016, **1**, 16021.
43. S. Nie and S. R. Emory, *Science*, 1997, **275**, 1102-1106.
44. X. Z. Zheng, S. G. Meng, J. Chen, J. X. Wang, J. J. Xian, Y. Shao, X. Z. Fu and D. Z. Li, *J. Phys. Chem. C*, 2013, **117**, 21263-21273.
45. J. L. Yuan and C. J. Hao, *Sol. Energy Mater. Sol. Cells*, 2013, **108**, 170-174.
46. P. E. Blochl, *Phys. Rev. B*, 1994, **50**, 17953-17979.
47. G. Kresse and D. Joubert, *Phys Rev B*, 1999, **59**, 1758-1775.
48. J. P. Perdew, K. Burke and M. Ernzerhof, *Phys. Rev. Lett.*, 1996, **77**, 3865-3868.
49. S. R. Bahn and K. W. Jacobsen, *Comput. Sci. Eng.*, 2002, **4**, 56-66.
50. A. A. Peterson, F. Abild-Pedersen, F. Studt, J. Rossmeisl and J. K. Nørskov, *Energ Environ. Sci.*, 2010, **3**, 1311-1315.
51. M. Rahaman, A. Dutta, A. Zanetti and P. Broekmann, *ACS Catal.*, 2017, **7**, 7946-7956.
52. B. Chi, H. Lin and J. Li, *Int. J. Hydrogen Energy*, 2008, **33**, 4763-4768.
53. Y. Yang, F. Teng, Y. D. Kan, L. M. Yang, Z. L. Liu, W. H. Gu, A. Zhang, W. Y. Hao and Y. R. Teng, *Appl Catal B-Environ*, 2017, **205**, 412-420.
54. S. Rasul, D. H. Anjum, A. Jedidi, Y. Minenkov, L. Cavallo and K. Takanabe, *Angew. Chem. Int. Ed. Engl.*, 2015, **127**, 2174-2178.
55. J. Baltrusaitis, J. Schuttlefield, E. Zeitler and V. H. Grassian, *Chem Eng J*, 2011, **170**, 471-481.
56. M. F. Baruch, J. E. Pander, J. L. White and A. B. Bocarsly, *Acs Catal*, 2015, **5**, 3148-3156.
57. J. Baltrusaitis, J. H. Jensen and V. H. Grassian, *J Phys Chem B*, 2006, **110**, 12005-12016.

-
58. B. Smith, D. Irish, P. Kedzierzawski and J. Augustynski, *Journal of the Electrochemical Society*, 1997, **144**, 4288-4296.
 59. J. E. Pander, D. Ren, Y. Huang, N. W. X. Loo, S. H. L. Hong and B. S. Yeo, *ChemElectroChem*, 2018, **5**, 219-237.
 60. Y. Ichinohe, T. Wadayama and A. Hatta, *Journal of Raman Spectroscopy*, 1995, **26**, 335-340.
 61. A. Campion and P. Kambhampati, *Chem. Soc. Rev.*, 1998, **27**, 241-250.
 62. M. Morimoto, Y. Takatsuji, K. Hirata, T. Fukuma, T. Ohno, T. Sakakura and T. Haruyama, *Electrochim Acta*, 2018, **290**, 255-261.